buildings

MDPI

Article

Seismic Optimization of Fluid Viscous Dampers in Cable-Stayed Bridges: A Case Study Using Surrogate Models and NSGA-II

Qunfeng Liu [1,*], Zhen Liu [1], Jun Zhao [2], Yuhang Lei [1], Shimin Zhu [3] and Xing Wu [3]

[1] School of Architecture and Civil Engineering, Xi'an University of Science and Technology, Xi'an 710054, China; 22204053031@stu.xust.edu.cn (Z.L.); leiyuhanglyh@163.com (Y.L.)
[2] School of Science, Xi'an University of Architecture and Technology, Xi'an 710055, China; zjbridge@xauat.edu.cn
[3] CCCC First Highway Consultants Co., Ltd., Xi'an 710068, China; shimin_zhu@outlook.com (S.Z.); wuxing.cccc@outlook.com (X.W.)
* Correspondence: qliu@xust.edu.cn

Abstract: This study investigates two optimization strategies to enhance the seismic performance of cable-stayed bridges equipped with Fluid Viscous Dampers (FVDs). A detailed finite element model of a case study bridge was developed to evaluate the effectiveness of these strategies in optimizing FVD parameters for seismic mitigation. The first strategy employs a traditional parametric analysis approach, which identifies optimal parameters by examining their influence on seismic performance. The second strategy employs a data-driven surrogate model, specifically an Artificial Neural Network (ANN), integrated with the NSGA-II optimization algorithm. This surrogate model significantly reduced computational demands during the optimization process, offering a more efficient and scalable solution for the optimization process. Results demonstrate that the ANN-based approach effectively addresses multi-objective optimization challenges while providing a robust framework for improved seismic performance in cable-stayed bridges. These findings highlight the potential of the ANN-based strategy in the seismic optimization of FVD parameters for cable-stayed bridges.

Keywords: cable-stayed bridge; fluid viscous damper; parameter optimization; surrogate model; NSGA-II

check for updates

Academic Editor: Fabrizio Gara

Received: 4 April 2025
Revised: 19 April 2025
Accepted: 23 April 2025
Published: 24 April 2025

Citation: Liu, Q.; Liu, Z.; Zhao, J.; Lei, Y.; Zhu, S.; Wu, X. Seismic Optimization of Fluid Viscous Dampers in Cable-Stayed Bridges: A Case Study Using Surrogate Models and NSGA-II. *Buildings* **2025**, *15*, 1446. https://doi.org/10.3390/buildings15091446

Copyright: © 2025 by the authors. Licensee MDPI, Basel, Switzerland. This article is an open access article distributed under the terms and conditions of the Creative Commons Attribution (CC BY) license (https://creativecommons.org/licenses/by/4.0/).

1. Introduction

Cable-stayed bridges are widely utilized in modern long-span and landmark bridge engineering due to their excellent structural performance, notable spanning capacity, and aesthetic appeal. Based on the connection configurations between pylons and decks, cable-stayed bridges are categorized as fixed, partially floating, or floating systems. Floating systems, in particular, offer unique advantages for long-span bridges because of their remarkable spanning capacity and high flexibility [1], which significantly reduces seismic demands during near-fault earthquakes, providing exceptional seismic mitigation performance. However, the high flexibility of floating systems poses critical challenges under strong seismic events, as the absence of rigid pylon-deck connections often results in substantial deck displacements. This can lead to excessive deformation of the pylons or overstressing of their bases, ultimately threatening the structural integrity of bridges during seismic excitations [2–4].

In recent decades, extensive research focused on mitigating the excessive displacements in floating cable-stayed bridges under seismic loading. To enhance their seismic

performance, various pylon-deck connection devices have been proposed. These devices can be broadly categorized into two types: (1) isolation devices, such as elastic bearings and friction pendulum bearings, which extend the fundamental periods of bridges to reduce seismic demands [5–7], and (2) energy dissipation devices, such as viscous dampers and metallic dampers, which absorb seismic energy through material yielding or thermal dissipation [8].

Among these, Fluid Viscous Dampers (FVDs) demonstrate superior performance in vibration control, owing to their exceptional energy dissipation capabilities [9–11]. Extensive studies have highlighted the effectiveness of FVDs in reducing vibration amplitudes and seismic responses [12–16]. For instance, Zhu et al. [4] reported that nonlinear FVDs can reduce longitudinal deck displacement by up to 79% and tower bending moment by 56% in a cable-stayed bridge under randomly generated earthquakes. Furthermore, FVDs enhanced seismic performance without significantly altering the inherent stiffness of the structure, making them an adaptable and efficient solution for seismic response mitigation in cable-stayed bridges [4,17,18].

In the seismic design of long-span bridges, precise tuning of FVD parameters, particularly the velocity exponent (α) and damping coefficient (C), is essential for effective displacement control [19]. Feng et al. [20] demonstrated that the velocity exponent significantly influences displacement control, while the damping coefficient primarily governs energy dissipation efficiency. Wu et al. [21] conducted a parametric analysis of α and C to optimize multiple longitudinal seismic responses—namely, top displacement, base shear, and base moment of pylons—for the Xigu Yellow River cable-stayed bridge, showcasing the effectiveness of FVD optimization in achieving balanced seismic performance. Similarly, Wen et al. [22] utilized a genetic algorithm with parallel computation for multi-objective parameter optimization, aiming to minimize repair costs and enhance the seismic resilience of a benchmark cable-stayed bridge. Despite these advances, optimizing FVD parameters remains a considerable challenge, requiring the careful trade-off of multiple, often competing objectives, such as displacement control, stress mitigation, and structural feasibility [21–23].

In recent years, various methods have been proposed to enhance the efficiency of FVD parameter optimization. For example, He et al. [19] used the surface fitting function to optimize FVD parameters in a cable-stayed bridge under high-intensity seismic conditions, achieving a substantial reduction in the seismic response. Similarly, Xu et al. [23] employed the response surface method to identify optimal FVD parameters and validated their effectiveness in mitigating seismic responses through experimental testing. Liu et al. [24] developed a multi-objective optimization function for a single-pylon cable-stayed bridge based on the energy dissipation theory, which provided an optimal FVD parameter combination. While these studies achieved improvements in optimization efficiency, they were constrained by a limited number of design variables and struggled to identify optimal solutions within complex multi-objective optimization scenarios.

For multi-objective optimization design, data-driven optimization approaches have gained attention in recent engineering research. For instance, Chen et al. [25] utilized FEM simulations integrated with a response surface optimization algorithm to optimize the design parameters of link beams for seismic design of piers with varying heights. Similarly, Baei and Terzic [26] employed parallel computing and the multi-objective particle swarm optimization algorithm (MOPSO) to optimize viscous damper parameters, enhancing the seismic performance of a moment frame. Additionally, Sun et al. [27] applied the Extreme Gradient Boosting Tree (XGBoost) algorithm combined with the analytic hierarchy process to evaluate ultra-high-performance concrete, effectively balancing multiple design objectives.

In conventional multi-objective optimization methods, the evaluation of objectives mostly depends on computationally intensive FE simulations. These high computational

demands often hinds the exploration of high-dimensional design spaces, reducing the likelihood of identifying globally optimal solutions. To overcome this challenge, researchers have proposed some computationally efficient surrogate models as alternatives to FE simulations. For instance, Guo et al. [28] used an ANN-based surrogate model to accurately predict the design parameters of triple friction pendulum bearings (TFPBs) for high-speed railway bridges and derived the design parameters based on response evaluation. Fang et al. [29] developed a multi-objective optimization framework for hybrid-braced structures by integrating five distinct machine learning (ML) prediction models with the Non-Dominated Sorting Genetic Algorithm II (NSGA-II) to enhance design efficiency and performance. Jiang et al. [30] utilized the NSGA-II algorithm to optimize magnetorheological damper designs with a focus on two objectives, achieving effective trade-offs between mechanical and electromagnetic performance. Yang et al. [31] proposed an NSGA-II-based approach to optimize the repair sequencing of cable-stayed bridges within a three-objective framework. Similarly, Tian et al. [32] applied an improved NSGA-II to perform multi-objective optimization of cable forces in arch bridges.

Table 1 summarizes some state-of-the-art multi-objective optimization applications. While these studies demonstrate that NSGA-II is a robust algorithm for addressing multi-objective optimization due to its ability to identify Pareto-optimal solutions and maintain solution diversity, several critical challenges persist in optimizing FVD parameters. Specifically: (1) existing surrogate models struggle to achieve the necessary balance between accuracy and generalizability, which is crucial for reliability optimization results; (2) multi-objective optimization algorithms like NSGA-II necessitate numerous iterations per generation, making computationally intensive FE simulations impractical under tight time constraints. Furthermore, current research has explored only a limited range of design variables and typically restricted optimization objectives to no more than three, thereby constraining the optimization process. This indicates that state-of-the-art surrogate models often compromise either the accuracy or the generalizability of the optimization outcomes. Consequently, despite its potential, the application of NSGA-II for FVD parameter optimization in cable-stayed bridges remains underexplored. Addressing these challenges calls for the development of a computationally efficient, multi-task surrogate model to facilitate accurate and practical multi-objective optimization of FVD parameters.

This study aims to validate a robust multi-objective optimization strategy for the seismic design of FVDs in cable-stayed bridges. Two strategies are compared. The first relies on the parametric analysis of a cable-stayed bridge equipped with a single equivalent FVD, where optimal parameters are identified through engineering expertise. The second strategy leverages a data-driven surrogate model to accurately approximate seismic responses and pairs it with the NSGA-II optimization algorithm. This strategy reduces the dependency of forward evaluations on computationally intensive FE simulations during the optimization process, making it highly effective for tackling complex optimization problems involving multiple design parameters and objectives.

This paper is organized as follows: Section 2 describes the development of the finite element model for the cable-stayed bridge and provides details on the seismic input. Section 3 is dedicated to the analysis and optimization of FVD parameters through detailed parametric analysis. Section 4 introduces a surrogate model-based approach to optimize the FVD parameters for the case study bridge, utilizing an ANN surrogate model in combination with the NSGA-II. Finally, the paper concludes with a comparative analysis of the two-parameter optimization strategies.

Table 1. Review of state-of-the-art algorithms for multi-objective optimization.

Literature	Year	Optimization Strategy	Application
Xu et al. [23]	2019	FE model, parametric analyses	Parameter optimization of FVDs in cable-stayed bridges
Chen et al. [26]	2022	FE model, response surface method	Two-objective seismic optimization of design parameters in double-column piers
Baei et al. [27]	2022	FE model, MOPSO algorithm	Multi-objective optimization of damper parameters for viscous dampers in moment frames
Guo et al. [29]	2024	ANN model, response evaluation	TFPB parameter design based on ANN inverse prediction model in simply-supported bridges
Fang et al. [30]	2022	Five ML models, NSGA-II	Multi-objective optimization of brace design parameters in structures with hybrid braces
Jiang et al. [31]	2022	Design equations, NSGA-II	Multi-objective optimization of design parameters for a magnetorheological damper
Yang et al. [32]	2024	FE model, NSGA-II	Multi-objective optimization of repair sequence in cable-stayed bridges
Tian et al. [33]	2024	FE model, NSGA-II	Multi-objective optimization of cable forces in arch bridges

2. Methodology

This study focuses on optimizing the parameters of FVDs installed on a cable-stayed bridge by employing two distinct optimization strategies. As illustrated in Figure 1, the overall research framework is structured as follows:

(1) Finite element (FE) model development:

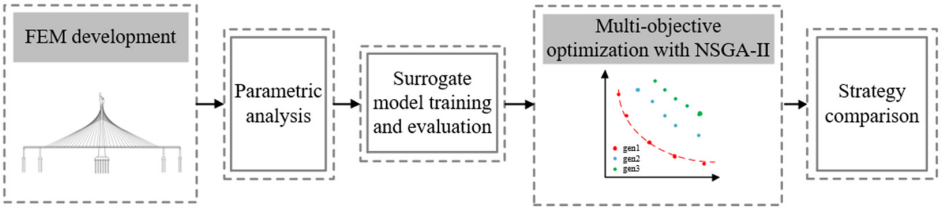


Figure 1. Optimization workflow of FVD damper parameters based on a surrogate model.

A detailed finite element model of the case study cable-stayed bridge is constructed. Representative ground motion records are selected as seismic inputs for the subsequent analysis and optimization tasks.

(2) Parametric analysis:

The seismic response of the case study bridge is evaluated under diverse combinations of FVD parameters. The relationships between damper parameters and seismic responses are analyzed to determine a practical range of design candidates.

(3) Surrogate model construction and evaluation:

A dataset is generated through nonlinear time-history analyses linking FVD parameters with seismic responses. Four machine learning models are trained and evaluated using metrics. The superior model (ANN) is selected to substitute computationally intensive FEM analyses during optimization.

(4) Multi-objective FVD optimization with NSGA-II:

The NSGA-II algorithm is utilized to solve a multi-objective optimization problem, aiming at three or four seismic performance objectives. Final optimal solutions are selected from the converged Pareto fronts.

(5) Comparison of optimization strategies:

The two optimization strategies, parametric analysis, and surrogate model-based op-timization, are compared in terms of their methodologies and the seismic responses of the bridge under the optimal parameters derived from each strategy.

2.1. Finite Element Model of the Case Study Cable-Stayed Bridge

The case study bridge is the Shijiazhuang Hutuo River Bridge, featuring a main span arrangement of 40 m + 150 m + 150 m + 40 m. It is a single-pylon cable-stayed bridge with uniquely twisted spatial stay cables symmetrically arranged on both sides of the pylon. The bridge deck comprises two separate steel box girders, each 29.5 m wide, connected by transverse girders spaced 8 m apart. The pylon is centrally located along the bridge's total longitudinal length and within the transverse girder spacing. The structural configuration and geometric dimensions are illustrated in Figure 2.

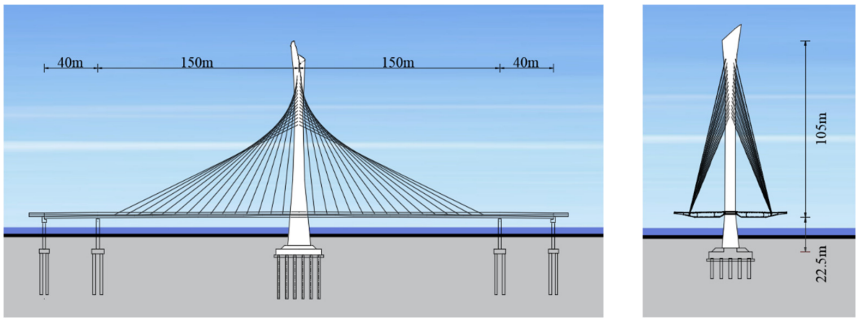


Figure 2. Hutuo River cable-stayed bridge: (**a**) longitudinal view; (**b**) transverse view.

This study develops a three-dimensional (3D) numerical model of the cable-stayed bridge using the OpenSees finite element framework (version 3.6.0) [33], as shown in Figure 3. The model represents the entire bridge structure, including two side spans and two middle spans, with 706 nodes and 707 elements. Specifically, the finite element configuration comprises 332 girder elements, 67 pylon elements, 62 cable elements, 204 rigid links, and 1 zero-length element. Elastic beam-column elements are used to model both the pylon and the longitudinal girders. Between the two longitudinal girders, there are forty transverse girder elements that connect to both longitudinal girders with eighty rigid links. The upper part of the pylon located above the deck is made of steel and is modeled with an elastic modulus of 2.06×10^{11} N/m^2, while the lower part of the pylon beneath the deck is made of concrete with an elastic modulus of 3.6×10^{10} N/m^2. The stay cables are represented by truss elements using the *steel02* material in OpenSees, characterized by an elastic modulus of 195 GPa and yield stress of 1.86 GPa. The 62 cables are connected to the pylon and the longitudinal girders with 124 rigid links on both ends. All the constitutive behaviors of these elements are illustrated in Figure 3.

The case study cable-stayed bridge is modeled as an ideal floating system. To control the displacements between the pylon and the longitudinal girders, an equivalent FVD is installed between the pylon and the girders, as illustrated in Figure 3. The equivalent FVD is based on the Maxwell viscoelastic model, which combines a linear spring with a nonlinear dashpot in series [4]. This model simplifies the analysis by reducing the design parameters to three: damper stiffness (K), damping coefficient (C), and velocity exponent (α), which are physically intuitive and easy to interpret. In the bridge's FE model, a single equivalent FVD is built with a zero-length element, and its mechanical behavior is governed by the Maxwell model. The piers beneath the side spans are modeled as roller supports that only permit longitudinal sliding.

After developing the FE model, the dynamic responses of the cable-stayed bridge equipped with FVDs were evaluated under various parameter combinations using nonlinear time-history analysis. To streamline the analysis, the pylon base was assumed to be fully fixed to the ground, thereby disregarding soil-structure interaction (SSI). Live load effects in both lateral and vertical directions were excluded from consideration in the dynamic

analysis, focusing solely on the seismic performance of the bridge [34]. Additionally, cable sag effects in the stay cables are omitted in this study to simplify the analysis. While structural nonlinearity and SSI are known to significantly influence the seismic behavior of long-span bridges under extreme loading conditions [4,35], their inclusion would introduce increased model complexity, computational demands, and uncertainties related to soil properties. As these factors are beyond the scope of this study, they were excluded from focusing on optimizing the FVD parameters and evaluating key superstructure responses to seismic excitation. Furthermore, the adoption of linear assumptions ensures consistency in comparison with results from previous studies [36].

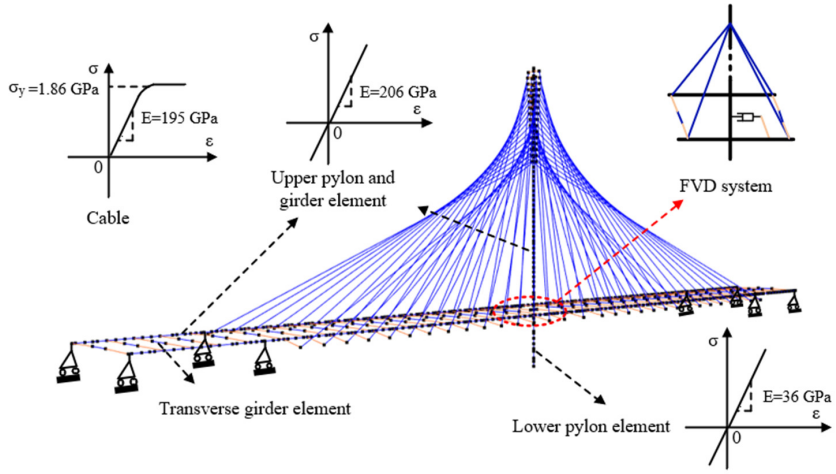


Figure 3. Finite element model of the case study cable-stayed bridge and the implementation of FVD system.

2.2. Construction of Surrogate Models

(1) Seismic performance evaluation indicators

The seismic performance evaluation indicators for the cable-stayed bridge in this study—longitudinal displacement of the deck, longitudinal top displacement of the pylon, and the base shear of the pylon—are key measures for understanding its behavior under seismic loads. Longitudinal deck displacement reflects the horizontal seismic response, deformation characteristics, and stiffness distribution of the bridge, highlighting the efficiency of the seismic design. The pylon's top displacement measures its deformation and structural stability, emphasizing the stiffness and load transmission of the pylon under earthquake actions. Base shear at the pylon's base provides insights into seismic force pathways and highlights the foundation's risk, particularly in understanding how forces are transmitted through the pylon to the substructure. Together, these indicators align with performance-based seismic design principles and provide a set of seismic performance indicators for a comprehensive evaluation of the cable-stayed bridge.

(2) Dataset construction of seismic responses

Based on the empirical design cases, the initial feasible variation ranges for the FVD parameters were determined, forming a three-dimensional design space. To efficiently explore this design space, the Latin Hypercube Sampling (LHS) method was employed to generate sample data due to its capacity to minimize parameter correlations, maintain statistical diversity, and reduce the required sample size. This approach ensured This approach ensured a comprehensive representation of the parameter distribution [37]. Here, each FVD, defined by a parameter combination (K, C, α), contains three design parameters. Using the LHS method, 1000 representative parameter combinations were generated ($10 \times 10 \times 10$). Nonlinear time-history analyses of the FVD-equipped bridge were then performed on the OpenSees

platform for each parameter combination to evaluate seismic responses. The damping parameters served as inputs, while seismic response indicators—longitudinal deck displacement (y_d), pylon top displacement (y_t), pylon base shear (y_s), and mean bending moment energy (y_e)—constituted the outputs, constructing the 'parameters—responses' dataset.

(3) Establishment and evaluation of surrogate models

Four machine learning frameworks such as Decision Tree (DT), Extreme Gradient Boosting (XGBoost), Random Forest (RF), and Artificial Neural Network (ANN) were selected as surrogate models to predict the seismic responses from the bridge with various FVD parameters. To ensure robust generalization to unseen data, the 'parameters—responses' dataset was divided into training, validation, and testing subsets. For the DT, RF, and XGBoost models, critical hyperparameters, including the number of decision trees, maximum tree depth, learning rate, number of base estimators, and minimum samples per split, were systematically optimized using the Optuna framework (version 1.4.0) [38], ensuring improved model accuracy and robustness. Similarly, for the ANN model, essential hyperparameters such as the number of layers, neurons per layer, and learning rate were fine-tuned to maximize the network's learning efficiency and generalization capabilities.

Model performance evaluation was conducted using five-fold cross-validation to minimize variability and ensure robust assessment. Metrics such as the coefficient of determination (R^2), Root Mean Squared Error (RMSE), and Mean Absolute Error (MAE) were calculated to provide a comprehensive evaluation of prediction accuracy. Results from both the training and testing phases were assessed to detect and mitigate overfitting and underfitting risks. Ultimately, the surrogate model with the best predictive performance was selected and applied to optimize the FVD parameter design.

2.3. Multi-Objective Optimization Using the NSGA-II Algorithm

Under seismic loading, significant relative displacement between the pylon and the deck of a floating-type cable-stayed bridge requires effective mitigation strategies, such as installing FVDs between the pylon and the deck. This study focuses on optimizing three key seismic performance objectives in the longitudinal direction: pylon top displacement, longitudinal deck displacement, and pylon base shear. To achieve this, the Non-Dominated Sorting Genetic Algorithm II (NSGA-II)—a powerful multi-objective optimization algorithm based on an elitist strategy—is employed. NSGA-II offers several advantages, including low computational complexity, fast optimization speed, high accuracy, and diverse solution sets, making it well-suited for multi-objective optimization [39]. In this study, NSGA-II is used to derive the Pareto front, representing optimal trade-off solutions for the three seismic objectives. From the Pareto front, an optimal solution is selected to balance the engineering demands for longitudinal deck displacement, pylon top displacement, and pylon base shear. The results demonstrate the effectiveness of NSGA-II in optimizing FVD parameters to address complex seismic performance demands.

2.4. Selection of Ground Motions

Near-fault ground motions pose significant challenges to flexible bridges such as long-span cable-stayed bridges. These challenges arise from their pronounced velocity pulse effects and high ground velocity-to-acceleration ratios, which focus energy predominantly in the low-frequency range (0.1–1.0 Hz) [40]. Notably, the natural frequencies of cable-stayed bridges often fall within 0.1–0.5 Hz. This study targets a longitudinal floating-type cable-stayed bridge that is especially sensitive to near-fault motions. Under such seismic conditions, the floating configuration leads to prominent longitudinal deck displacements and horizontal displacements at the pylon tops.

To ensure the analysis accurately reflects the seismic performance of the case study cable-stayed bridge, near-fault earthquake records were carefully selected. Seven representative near-fault ground motion records were chosen from the Pacific Earthquake Engineering Research Center (PEER) database, encompassing a diverse range of tectonic environments to account for variability in seismic hazards. The key ground motion characteristics, summarized in Table 2, include parameters such as earthquake magnitude, the average shear wave velocity of the top 30 m of soil (Vs_30), peak ground acceleration (PGA), and peak ground velocity (PGV). The selected records have PGA values ranging from 0.28 g to 1.43 g.

Table 2. Selected near-fault ground motion records.

No.	Event	Year	Station	Magnitude	Vs_30 (m/s)	PGA (g)	PGV (cm/s)
1	Imperial Valley-06	1979	Chihuahua	6.53	242.05	0.28	30.5
2	Loma Prieta	1989	BRAN	6.93	476.54	0.64	55.9
3	Cape Mendocino	1992	Cape Mendocino	7.0	514	1.43	119.5
4	Northridge-01	1994	LA—Sepulveda VA	6.7	380	0.73	70.1
5	Kocaeli, Turkey	1999	Yarimca	7.5	297	0.31	73
6	Chi-Chi, Taiwan	1999	TCU084	7.6	553	1.16	115.1
7	Denali, Alaska	2002	TAPS Pump Sta. #10	7.9	553	0.33	126.4

According to the Chinese Guidelines for Seismic Design of Highway Bridges [41] and the seismic hazard report for the target bridge site, the design seismic level is defined by a PGA of 0.20 g and a characteristic period of 0.4 s. The site is classified as Type II within a seismic zone of 8 degrees defined by Chinese codes. To account for local hazard conditions, the selected seven ground motion records were scaled to a PGA of 0.20 g. This scaling aligns with the dynamic characteristics and seismic site conditions of the case study bridge. After amplitude adjustments, the scaled ground motions were utilized to develop the design response spectrum, as illustrated in Figure 4 [42]. Given the bridge's pronounced sensitivity to longitudinal displacements, the seismic analysis was conducted exclusively under longitudinal seismic excitations to capture its critical dynamic response.

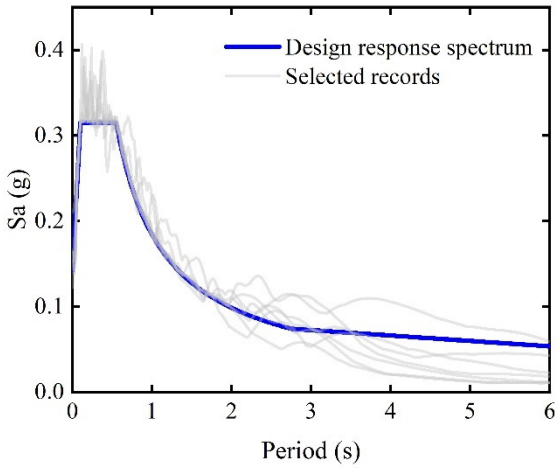


Figure 4. Acceleration spectra for the scaled ground motions.

3. Results and Discussion

3.1. Optimization of FVD Based on Parametric Analysis

3.1.1. Parametric Analyses of FVDs

In the seismic design of the case study cable-stayed bridge, an equivalent FVD is installed between the pylon and the girders. The design parameters of the equivalent FVD include damping coefficient (C), velocity exponent (α), and damper stiffness (K). For the sensitivity analysis of these parameters regarding structural seismic responses, an equally spaced sampling approach was utilized across their respective ranges. The damping coefficient (C) was set between 1000 and 10,000 kN/(m/s), with intervals of 1000 kN/(m/s). The velocity exponent (α) varied from 0.1 to 1.0, with intervals of 0.1, while the damper stiffness (K) ranged between 1×10^5 and 1×10^6 kN/m, with intervals of 1×10^5 kN/m. Using the identical design response spectrum, the seismic responses of the case study bridge equipped with FVDs were evaluated under various parameter combinations, with a focus on three critical performance metrics: longitudinal deck displacement, pylon top displacement, and pylon base shear.

Figures 5–7 illustrate the variations in the three seismic responses under the influence of different FVD parameters (K, C, and α). It can be observed that all three seismic responses are nearly insensitive to changes in damper stiffness. Specifically, as damper stiffness increases from 2×10^5 kN/m to 1×10^6 kN/m, the seismic responses exhibit a slight decrease. This observation aligns with previous studies [43] that indicate damper stiffness exerts a negligible influence on the seismic performance of bridges. Building on these findings, a damper stiffness (K) within the range of 8×10^5 to 1×10^6 kN/m is recommended.

In contrast, the velocity exponent and damping coefficient show a stronger correlation with these responses, consistent with findings from previous reports [4,44]. More specifically, both deck displacement and pylon top displacement decrease with an increase in C, but increase with a higher α. Conversely, the pylon base shear exhibits the opposite trend: it increases with increasing C and decreases with increasing α. Notably, when C is as low as 1000 kN/(m/s), the deck displacement and base shear increase significantly, while the pylon top displacement decreases remarkably, as illustrated in Figure 6. This suggests that the damping effect diminishes and becomes localized around the pylon-deck connection. Therefore, a damping coefficient of C = 1000 kN/(m/s) is excluded from the design range of damper parameters.

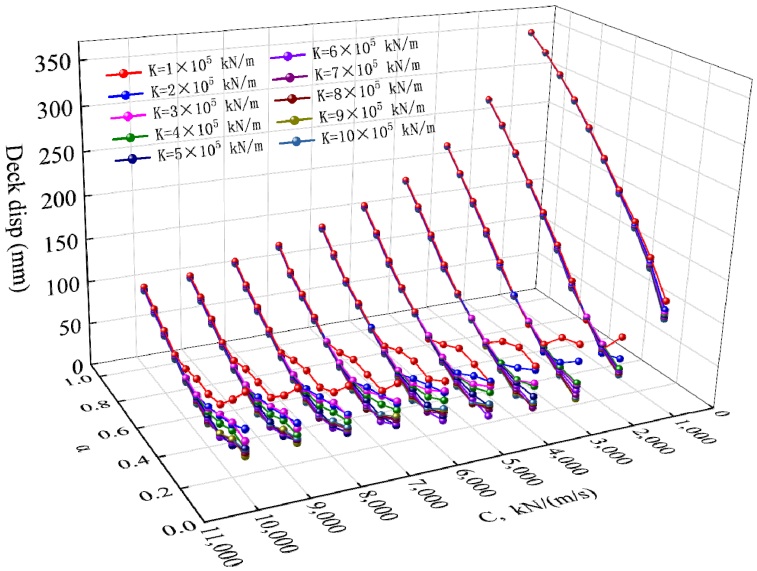


Figure 5. Longitudinal deck displacement as a function of *C* and α across different damper stiffnesses.

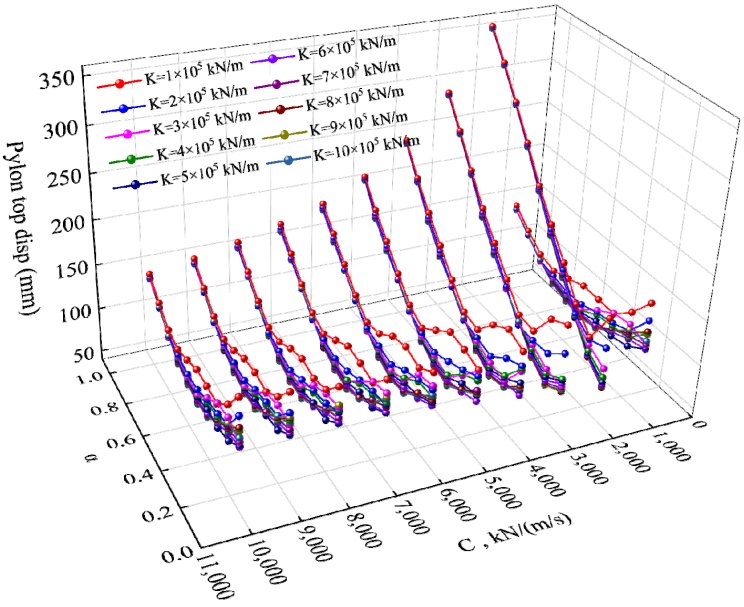


Figure 6. Pylon top displacement as a function of *C* and *α* across different damper stiffnesses.

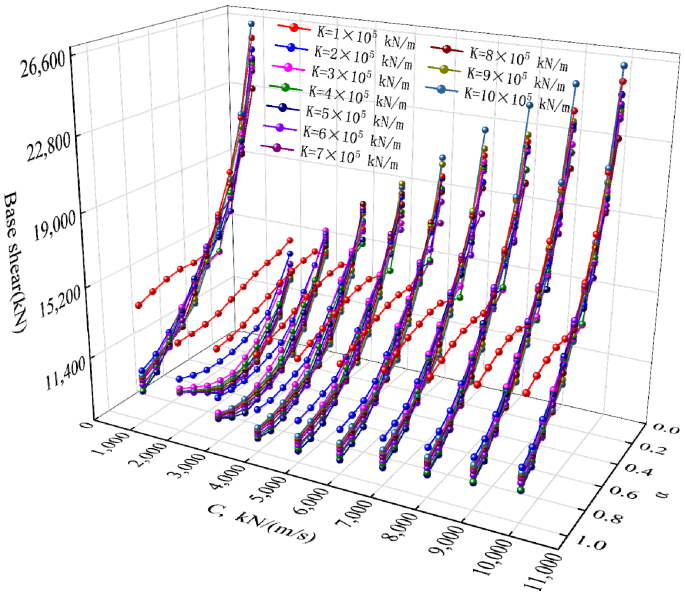


Figure 7. Pylon base shear as a function of C and *α* across different damper stiffnesses.

3.1.2. Optimal Design Spaces for Damper Parameters

To consider the importance of each response, all responses corresponding to each parameter combination are first normalized. In this study, Min-Max normalization is employed to scale the data to a uniform range of [0, 1]. This normalization addresses the issue of dimensional inconsistencies among the various responses [45] that are calculated in different units. Furthermore, this allows the adaptive weighting of these responses based on their relative importance, ensuring a balanced consideration in subsequent parametric analyses. Then, the summation of the normalized responses g ($=\Sigma\omega_i R_i$) is determined based on the normalized responses and expressed as Equation (1):

$$g = \frac{1}{n}\sum_{i=1}^{n}\omega_i R_i = \frac{1}{n}\sum_{i=1}^{n}\omega_i \frac{r_i - Min(r_i)}{Max(r_i) - Min(r_i)} \quad (1)$$

where R_i represents the i-th normalized response (i = 1, 2, …, n); n is the number of considered responses; ω_i represents the weight of the i-th response; r_i is the i-th original response; Min(r_i) and Max(r_i) denote the minimum and maximum values, respectively, of the i-th original responses across all data points.

This approach transforms the multi-objective optimization problem into a weighted sum of the multiple objectives [46]. By minimizing the single optimization function g, the overall optimization can be achieved. During parametric analysis, the corresponding g value was calculated for each parameter combination. The top ten smallest g values were selected, and the ten corresponding parameter combinations are presented in Table 3. From Table 3, it is observed that the velocity exponent falls in the range from 0.2 to 0.5, the damper stiffness from 8×10^5 to 1×10^6 kN/m, and the C from 3000 and 6000 kN/(m/s). These ranges are consistent with the results depicted in Figures 5–7.

Table 3. Optimal damping parameter combinations.

Velocity Exponent	Damper Stiffness (kN/m)	Damping Coefficient kN/(m/s)	Deck Disp. (mm)	Pylon Top Disp. (mm)	Pylon Base Shear (kN)	g
0.3	1×10^6	3000	54.7	92.3	10,847.8	0.276
0.2	1×10^6	3000	40.0	77.1	12,431.5	0.278
0.3	9×10^5	3000	54.4	91.6	10,971.7	0.280
0.2	9×10^5	3000	40.4	76.9	12,536.9	0.281
0.4	1×10^6	4000	55.9	93.6	10,858.8	0.283
0.3	1×10^6	4000	41.6	81.2	12,310.3	0.284
0.3	8×10^5	3000	54.5	91.8	11,125.0	0.286
0.4	1×10^6	5000	45.8	86.3	11,901.9	0.288
0.4	9×10^5	4000	55.9	93.1	11,011.6	0.288
0.5	1×10^6	6000	51.2	90.4	11,463.3	0.291

Figure 8 illustrates the three crucial responses within a multi-objective design space. In this space, a red point represents a response combination derived from the bridge equipped with a specific parameter combination. The blue points represent the ten selected responses that meet the minimization of the function g. It is observed that, in this case study, the optimal response combination can be clearly observed because the pylon top displacement and deck displacement are correlated with each other. From the blue points, the corresponding damper parameter combinations can be determined.

The three normalized responses, R_i, are mapped onto a two-dimensional space defined by C and α, both of which significantly influence the structural response, as shown in Figure 9. To achieve lower deck and pylon top displacements, the optimal parameter space lies in the upper-left region of the C-α space, where C takes a larger value while α is smaller. In contrast, to minimize the pylon base shear, the optimal parameter space shifts to the lower-right region of the C-α space, where C takes a smaller value and α is larger.

Figure 9d illustrates the preferred parameter space of the damper based on the sum of the three normalized responses, g, under the assumption of equal weighting ($\omega_1 = \omega_2 = \omega_3 = 1.0$). The blue region in the figure indicates the global optimal range for the combined responses, corresponding to a C range of 2000 to 7000 kN/(m/s) and an α range of 0.2 to 0.5. As shown in Figures 5–7, higher damping stiffness effectively suppresses structural responses. Notably, this parameter selection region is consistent with the optimal ranges suggested by Table 3.

This parametric analysis-driven optimization method is straightforward and allows for intuitive interpretation. However, it has several notable limitations. First, the parameter sampling is non-uniform and depends on empirically predefined samples, which may restrict the exploration of the design parameter space. Second, due to data constraints, an

exhaustive analysis of the design parameter space is not feasible, making it challenging to pinpoint the precise optimal damper parameters. As a result, while this approach offers valuable preliminary guidance for parameter selection, further optimization is necessary to improve accuracy and ensure practical applicability.

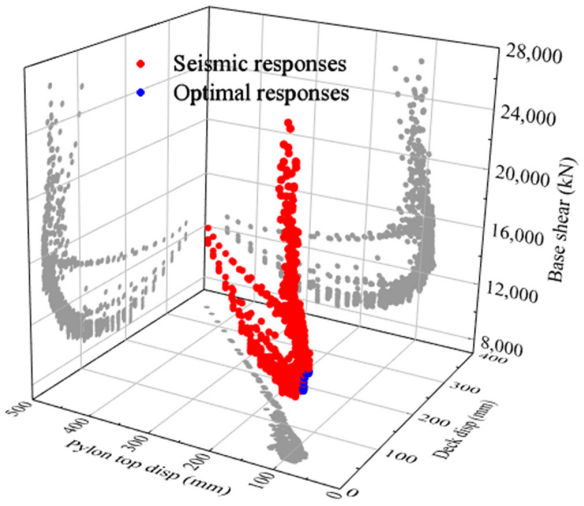


Figure 8. Multi-objective design space for three key structural responses.

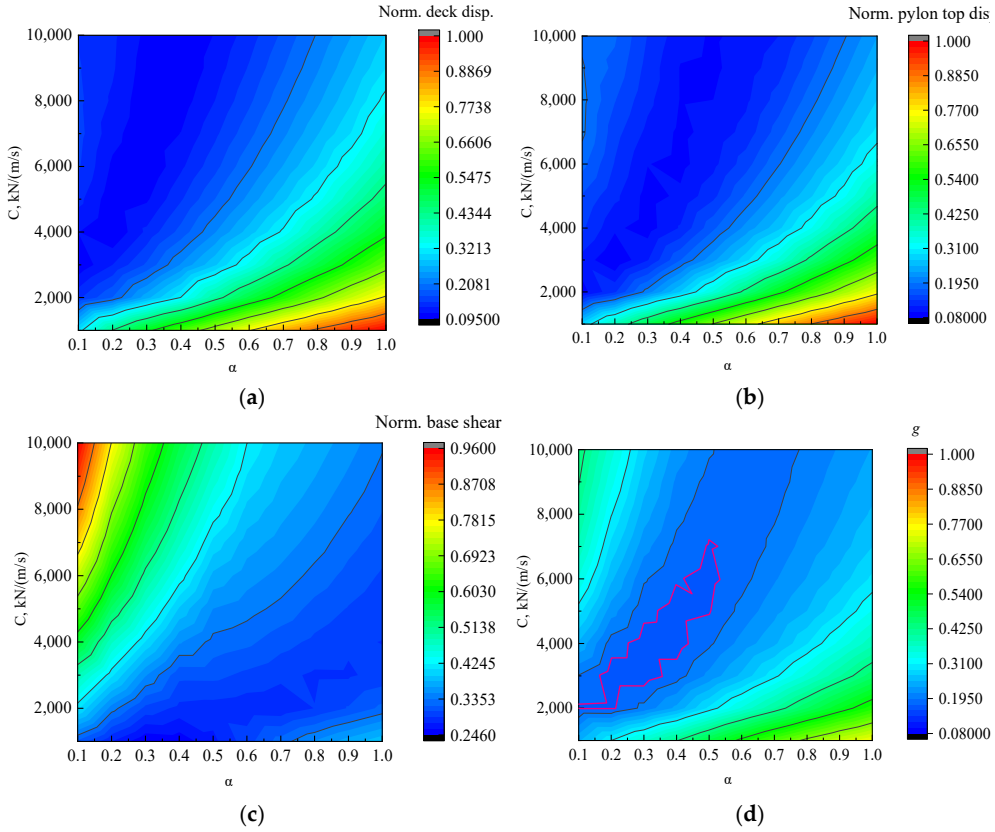


Figure 9. Projection of normalized responses onto the design space defined by C and α: (**a**) deck displacement, (**b**) pylon top displacement, (**c**) pylon base shear, and (**d**) the summation of the three normalized responses.

3.1.3. Seismic Mitigation of the Case Study Bridge

Figure 10 illustrates the time histories of three key structural responses of the case study bridge equipped with or without FVDs at the selected optimal parameter combination ($\alpha = 0.3$, $K = 1 \times 10^6$ kN/m, $C = 3000$ kN/(m/s)) under the design earthquake. In the figure,

blue lines represent the time-history responses of the undamped bridge (without FVDs), while red lines depict those obtained with the optimized FVDs. The responses—longitudinal deck displacement, pylon top displacement, and pylon base shear—are reduced to 54.7 mm, 92.3 mm, and 10,847.8 kN, respectively, after the installation of FVDs. These results demonstrate that incorporating the optimally tuned FVDs significantly enhances the seismic performance of the case study bridge by effectively mitigating key seismic responses. Compared to the case study bridge without FVDs, the pylon top displacement experiences the largest reduction, decreasing by 88.3%. Similarly, the longitudinal deck displacement is reduced by 85.0%, and the pylon base shear decreases by 25.7%. These findings highlight the effectiveness of the optimized FVD parameters in controlling critical structural responses under seismic loading. Moreover, the observed effectiveness is consistent with findings from previous studies [4,47].

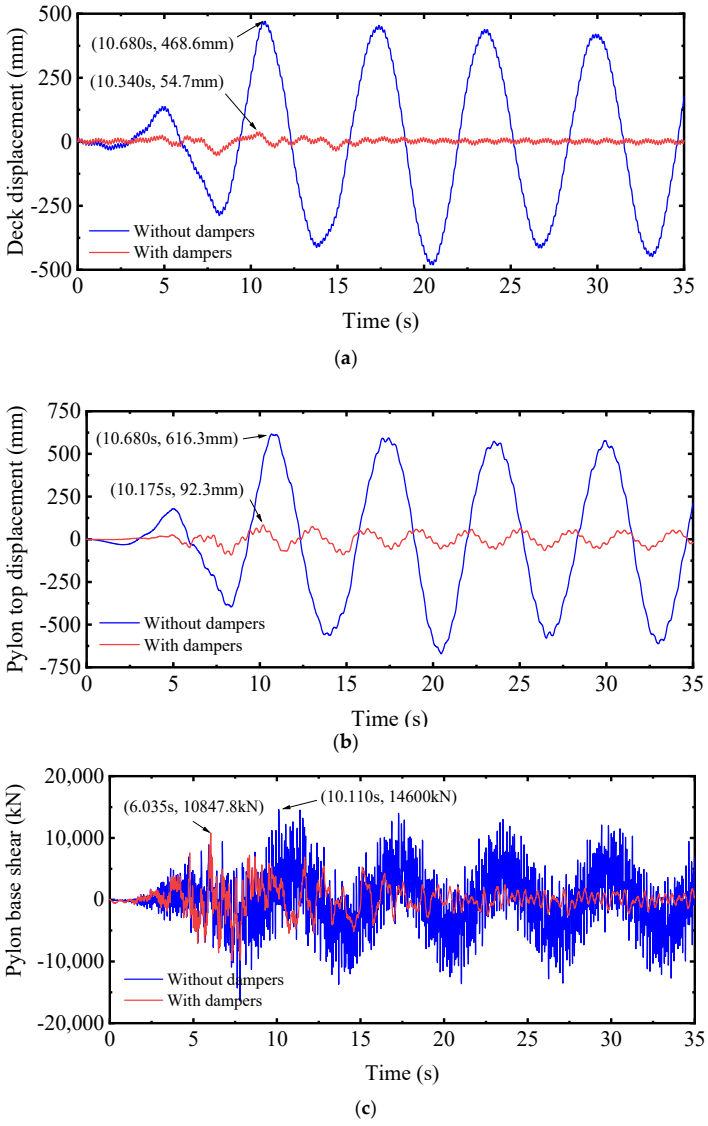


Figure 10. Time histories of (**a**) the longitudinal deck displacement, (**b**) the pylon top displacement, and (**c**) the pylon base shear for the case study bridge subjected to the design earthquake.

3.2. Surrogate Model-Based Parameter Optimization for FVDs

3.2.1. Dataset Generation

In this study, the seismic design of the case study bridge was optimized by calibrating the parameters of its FVDs. The selected FVD parameters included stiffness (K), damping

coefficient (C), and velocity exponent (α). The design space for these three parameters aligns with the parameter sensitivity analysis strategy, with K ranging from 1×10^5 to 1×10^6 kN/m, C ranging from 1×10^3 to 1×10^4 kN/(m/s), and α ranging from 0.1 to 1.0. A total of 1000 parameter combinations were produced using the LHS method. For each combination, nonlinear time-history analyses were performed on FE models of the cable-stayed bridge equipped with FVDs, producing its responses under near-fault seismic excitations over a duration of 35 s. The key responses analyzed included longitudinal deck displacement, pylon top displacement, pylon base shear, and bending moments at all deck and pylon nodes. Additionally, the mean bending moment energy (MBME) of the bridge elements was calculated using Equation (2):

$$\mathrm{MBME} = \frac{1}{m}\sum_{i=1}^{m}\frac{l_i}{4E_iI_i}\left({}^{L}M_i^2 + {}^{R}M_i^2\right) \tag{2}$$

where m represents the total number of structural elements; l_i, E_i, I_i,${}^{L}M_i$, and ${}^{R}M_i$ denote the length, elastic modulus, bending moment of inertia, left-node bending moment, and right-node bending moment of the i-th element in the decks and pylons, respectively.

The peak values of deck displacement, pylon top displacement, and pylon base shear of the case study bridge undergoing a 35 s duration of ground motion are selected as the key seismic performance indicators. Additionally, MBME reflects mechanical rationality in terms of material usage and strength demand, whereas a lower MBME indicates reduced economic and strength requirements. Therefore, MBME can serve as an additional performance indicator, contributing to structural optimization in seismic design. A total of 1000 parameter-responses datasets were generated, with each dataset containing three critical FVD parameters and four output responses.

3.2.2. Training of Surrogate Models

Four types of machine learning models such as DT, XGBoost, RF, and ANN were constructed. All models utilized the identical dataset generated from the FE simulations. The dataset was randomly divided into three subsets: 70% for training, 15% for validation, and 15% for testing.

To fully leverage the potential of the DT, XGBoost, RF, and ANN models, we employed Optuna, an automated hyperparameter tuning framework, to fine-tune their hyperparameters. For the DT and XGBoost models, the respective search spaces for hyperparameter tuning are detailed in Tables 4 and 5. Using RMSE and MAE as evaluation metrics, the Optuna framework was employed to automatically optimize critical hyperparameters, such as the maximum depth (max_depth), the minimum number of samples required to split a node (min_samples_split), and the minimum number of samples required at a leaf node (min_samples_leaf) for the DT model. Similarly, key hyperparameters for the XGBoost model, including the number of estimators (n_estimators), the number of layers (n_layers), learning rate, subsampling ratio (subsample), and column subsampling by tree (colsample_bytree), were optimized. The finalized optimal hyperparameters are presented in Tables 4 and 5.

Table 4. Optimal DT hyperparameters and search ranges.

Hyperparameter	Optimal Value	Search Range
max_depth	17	1–20
min_samples_split	5	1–10
min_samples_leaf	2	1–10

Table 5. Optimal XGBoost hyperparameters and search ranges.

Hyperparameter	Optimal Value	Search Range
n_estimators	85	10–200
n_layers	6	3–10
learning_rate	0.1	0.01–0.1
subsample	0.9	0.6–1
colsample_bytree	0.9	0.6–1

For the RF model, we defined a search space for the hyperparameters (see Table 6) and evaluated performance using RMSD and MAE metrics. Optuna utilizes a Bayesian optimization algorithm implemented via the Tree-structured Parzen Estimator (TPE) to optimize key hyperparameters, such as the number of decision trees (n_estimators), maximum tree depth (max_depth), and the minimum number of samples required to split a node (min_samples_split), among others. This Bayesian approach effectively balances exploration and exploitation by constructing a probabilistic model of the objective function, enabling the algorithm to converge toward optimal hyperparameter settings within a limited number of iterations. The optimal hyperparameters identified for the RF model are presented in Table 6.

Table 6. Optimal RF hyperparameters and search ranges.

Hyperparameter	Optimal Value	Search Range
n_estimators	34	10–100
max_depth	5	3–10
min_samples_split	3	1–10
min_samples_leaf	1	1–10
bootstrap	True	—

Similarly, for the ANN model, the hyperparameter search space was defined to include the number of layers (n_layers), the number of neurons per layer (hidden_layer_size), and the learning rate, as outlined in Table 7. Using RMSE and MAE as evaluation metrics, Optuna was employed to automate the optimization of these hyperparameters. The resulting optimized hyperparameters for the ANN model are summarized in Table 7. The proposed ANN model, as depicted in Figure 11, is designed with three input features and four output features. Its architecture comprises four hidden layers with 16, 32, 64, and 32 neurons, respectively. Before training, input data were preprocessed using Min-Max normalization. The ReLU activation function was employed across all hidden layers to ensure nonlinear transformations. For training, the Adam optimizer was utilized with a learning rate of 0.008 and a maximum of 3000 iterations, enabling efficient convergence of the model.

Table 7. Optimal ANN hyperparameters and search ranges.

Hyperparameter	Optimal Value	Search Range
hidden_layer_size	16, 32, 64, 32	10–100
n_layers	4	2–5
activation	ReLU	—
solver	Adam	—
α	0.0001	0.1–0.00001
learning_rate	0.008	—

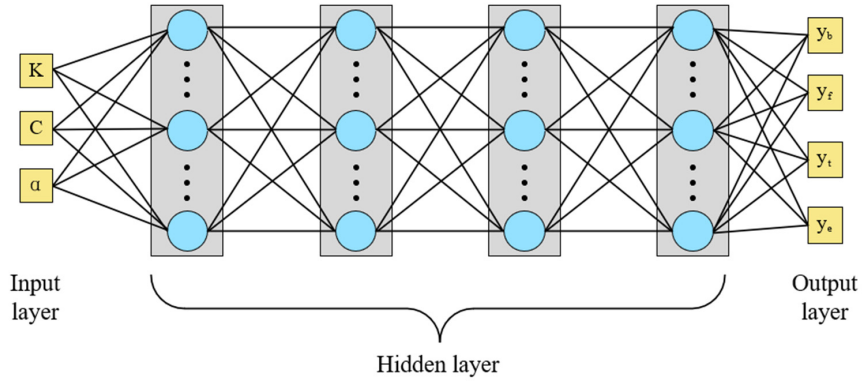


Figure 11. Architecture of the ANN prediction model.

3.2.3. Loss Function

To enhance the performance of the ANN model, this study employs the Mean Squared Error (MSE) as the loss function for each task. Specifically, the ANN model defines three separate loss components for the primary objectives: longitudinal deck displacement (L_1), pylon top displacement (L_2), and pylon base shear (L_3). Given that these three tasks are treated as equally important, their loss function weights are set identically ($\lambda_1 = \lambda_2 = \lambda_3$). In addition, an auxiliary task is incorporated to predict the mean bending moment energy, with its corresponding loss component (L_4). This auxiliary loss not only quantifies a key structural response but also serves as a regularization term, effectively balancing the contributions of the individual tasks during training.

To ensure consistency in magnitude across task-specific losses, the raw data were normalized prior to training. Here, we employed a weighted aggregation method to combine multiple losses into a single total loss, defined as $L_t = \sum \lambda_i L_i$ (i = 1, 2, 3, 4), where λ_i and L_i represent the weight and loss of the i-th task, respectively. The weighting scheme was subject to the constraints: $\lambda_1 = \lambda_2 = \lambda_3$ and $\lambda_1 + \lambda_2 + \lambda_3 + \lambda_4 = 4$. Under these constraints, we investigated the evolution of the total losses for various weight combinations. Figure 12 illustrates the evolution of the total training and validation loss over iterations for a specific weighting scenario (λ_1:λ_2:λ_3:λ_4 = 1:1:1:1). The figure shows that the total losses decrease rapidly at the beginning, converge gradually as training progresses, and stabilize after reaching an inflection point.

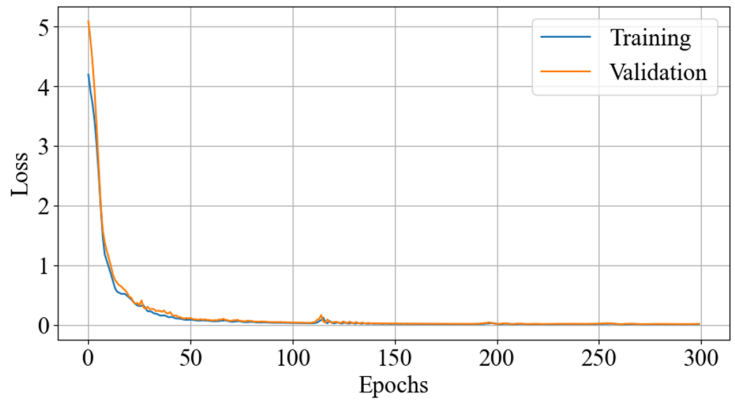


Figure 12. The total losses of the ANN model during training and validation processes.

Table 8 summarizes the key characteristics of the loss variation curves for different weight combinations. The results reveal that the optimal configuration is achieved with a weight ratio of λ_1:λ_2:λ_3:λ_4 = 1:1:1:1. In this setup, the model exhibits the most rapid convergence, marked by an inflection point at approximately 50 epochs. Furthermore, this

combination achieves the lowest total training and validation losses, with a training loss of 0.012 and validation loss of 0.015, outperforming all other tested combinations. This indicates that aligning the weight of the MBME loss with those of the structural response losses significantly enhances the convergence rate of the ANN model.

Table 8. Characteristics of the total loss variation curves for different weight combinations.

λ_1:λ_2:λ_3:λ_4	Inflection (Epochs)	Total Training Loss	Total Validation Loss
1.3:1.3:1.3:0.1	100	0.020	0.031
1:1:1:1	**50**	**0.012**	**0.015**
2/3:2/3:2/3:1	100	0.015	0.019
1/3:1/3:1/3:3	100	0.020	0.025
0.1:0.1:0.1:3.7	100	0.015	0.020

3.2.4. Evaluation of Surrogate Models

To evaluate the predictive accuracy and generalization capability of the models, three performance metrics were employed: RMSE, MAE, and R^2. The formulas for these metrics are provided below as Equations (3)–(5):

$$\mathrm{RMSE} = \sqrt{\frac{1}{n}\sum_{i=1}^{n}\left(y_i - \hat{y_i}\right)^2} \tag{3}$$

$$\mathrm{MAE} = \frac{1}{n}\sum_{i=1}^{n}\left|y_i - \hat{y_i}\right| \tag{4}$$

$$R^2 = 1 - \frac{\sum_{i=1}^{n}\left(y_i - \hat{y_i}\right)^2}{\sum_{i=1}^{n}\left(y_i - \overline{y}\right)^2} \tag{5}$$

In these equations, y_i represents the true value of the i-th output, $\hat{y}_i$ is the corresponding predicted value, n is the total number of data points, and $\bar{y}$ denotes the mean of the true values. RMSE and MAE are essential metrics for assessing model error, with lower values reflecting better predictive performance. In contrast, R^2 measures the proportion of variance in the true values that is explained by the predicted values, with values closer to 1.0 indicating a better model fit.

Figure 13 represents the prediction accuracies of four output features for the RF and ANN surrogate models. The horizontal axis represents the ground truth values from FE simulations, while the vertical axis depicts the values predicted by the surrogate models. Data points for both models align with the y = x line, indicating high predictive accuracy.

As summarized in Table 9, all models achieve high prediction accuracy on multiple tasks. Notably, the ANN model outperforms the DT, XGBoost, and RF models, achieving high accuracies above 98% across all tasks. Furthermore, the ANN model exhibits considerably lower RMSE and MAE values compared to the DT, XGBoost, and RF models. These findings affirm the ANN model's precision and validity as the surrogate model for subsequent parameter optimization.

To evaluate the model's predictive performance on unseen data, we employed a five-fold cross-validation procedure. Specifically, the training dataset was randomly segmented into five equal folds; one served as the validation set while the other four were used for training. We computed the evaluation metrics such as MAE, RMSE, and R^2 across all folds to ensure a robust assessment of the model's performance. Figures 14–17 display the ANN model's performance for four prediction tasks: longitudinal deck displacement, pylon top displacement, pylon base shear, and mean bending moment energy, respectively. Radar charts indicate that both RMSE and MAE values remain consistently low across all folds,

while the average R^2 value is approximately 0.99 with a standard deviation of ±0.01. These results demonstrate that the ANN model exhibits excellent generalization capabilities, confirming its suitability for parameter optimization tasks.

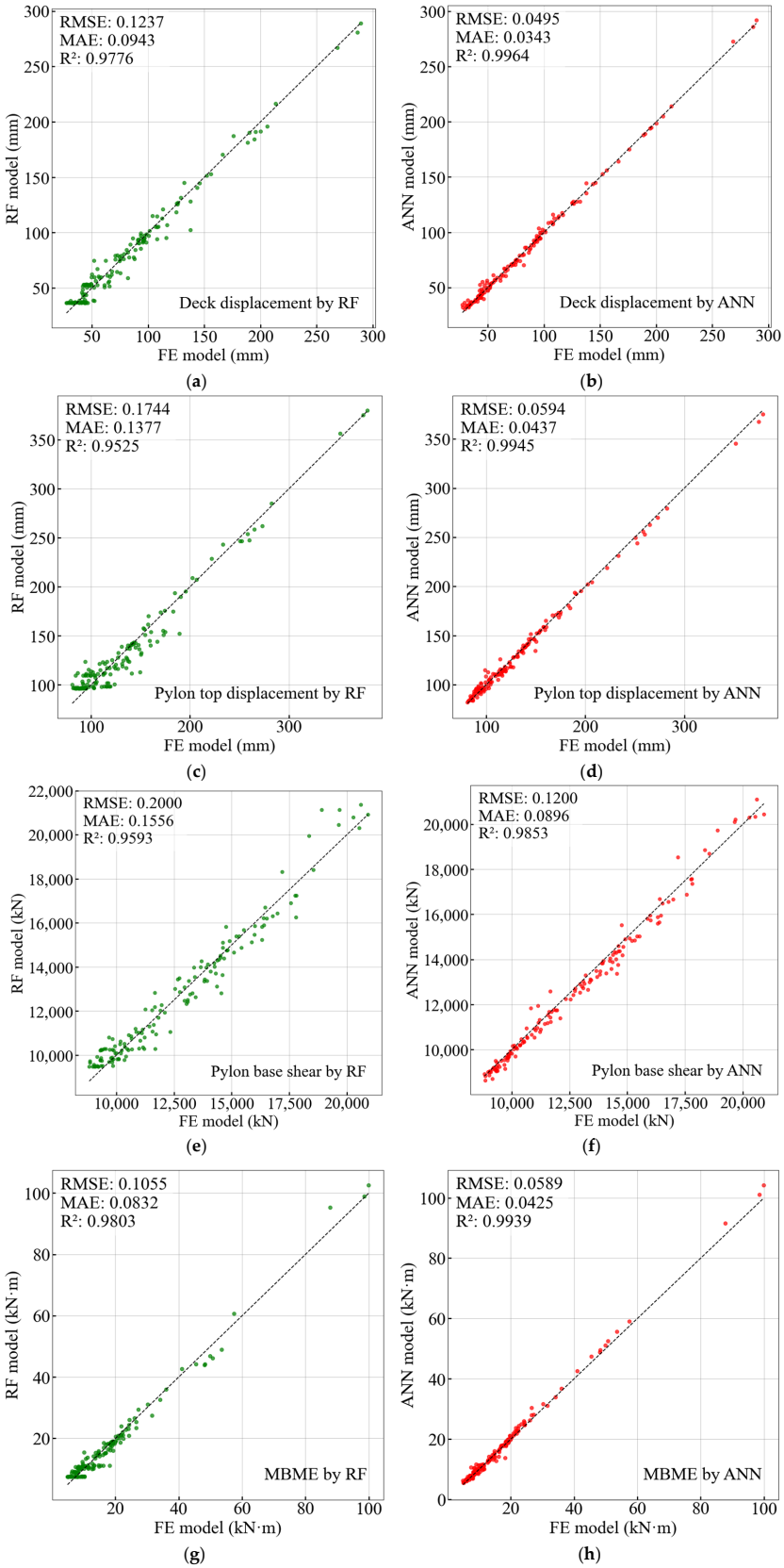


Figure 13. Comparison of prediction accuracy of (**a**,**b**) deck displacements, (**c**,**d**) pylon top displacement, (**e**,**f**) pylon base shear, and (**g**,**h**) MBME using RF and ANN models.

Table 9. Performance evaluation metrics of the DT, XGBoost, RF, and ANN surrogate models.

Model	Metrics	Deck Disp.	Pylon Top Disp.	Pylon Base Shear	MBME
DT	RMSE	0.140	0.161	0.234	0.105
	R^2	0.971	0.960	0.944	0.981
	MAE	0.094	0.106	0.174	0.067
XGBoost	RMSE	0.187	0.233	0.228	0.211
	R^2	0.948	0.915	0.947	0.922
	MAE	0.125	0.157	0.168	0.121
RF	RMSE	0.148	0.187	0.206	0.153
	R^2	0.979	0.967	0.951	0.979
	MAE	0.112	0.146	0.159	0.153
ANN	RMSE	0.060	0.069	0.124	0.058
	R^2	**0.995**	**0.993**	**0.984**	**0.994**
	MAE	0.044	0.047	0.080	0.039

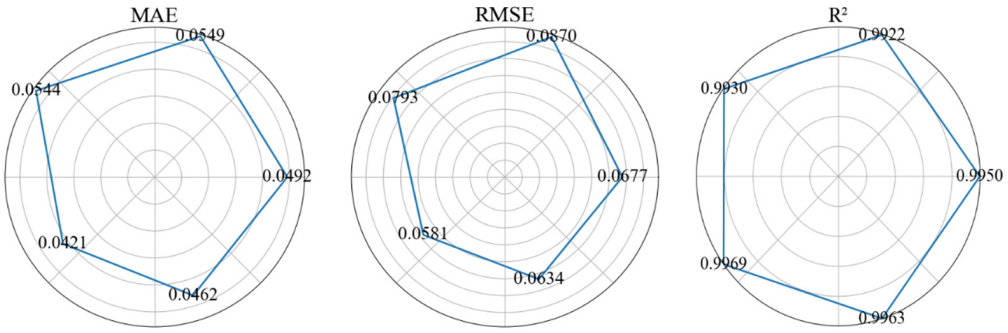


Figure 14. Evaluation metrics of five-fold cross-validation for longitudinal deck displacement.

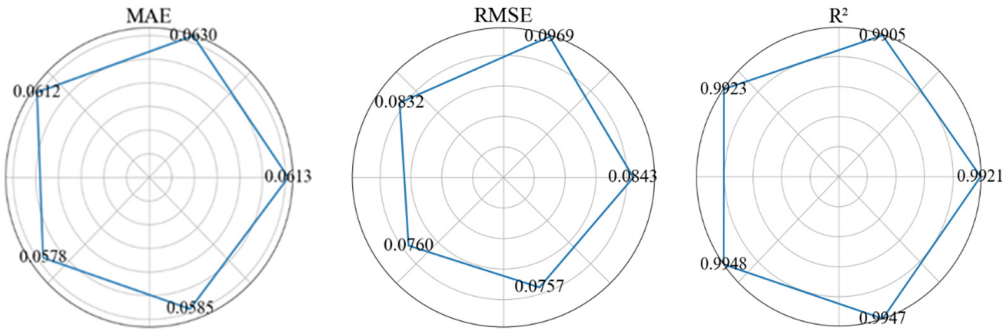


Figure 15. Evaluation metrics of five-fold cross-validation for pylon top displacement.

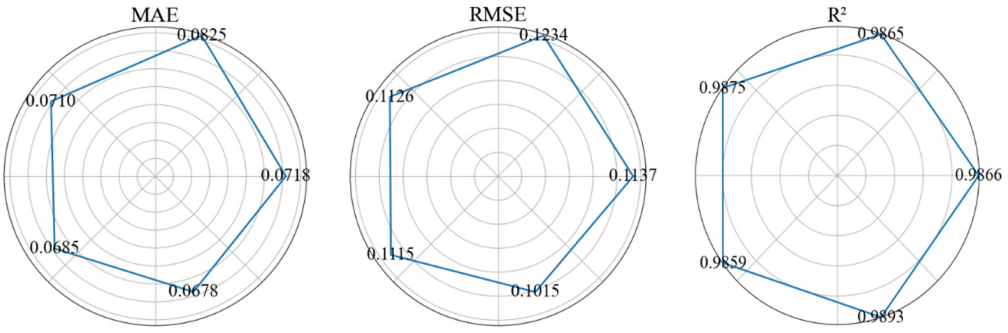


Figure 16. Evaluation metrics of five-fold cross-validation for pylon base shear.

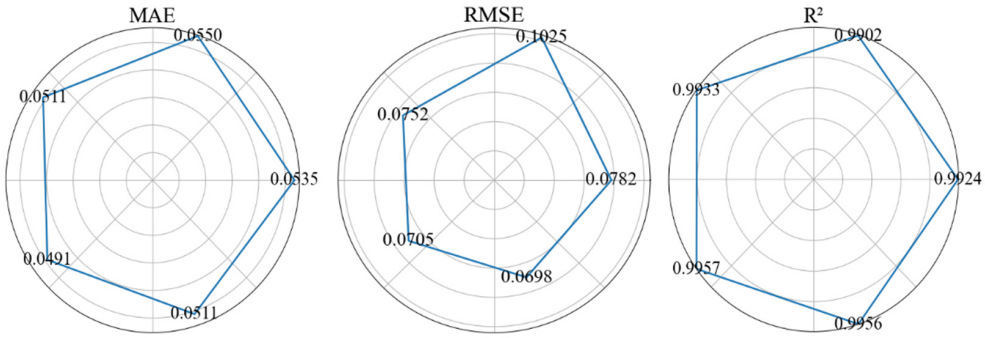


Figure 17. Evaluation metrics of five-fold cross-validation for mean bending moment energy.

3.2.5. Optimization of Damping Parameters Based on the ANN Model

In this study, the NSGA-II algorithm was employed to perform multi-objective optimization of FVD parameters. A population size of 200 was chosen to ensure adequate diversity and thorough exploration of the design space. For each generation, the structural responses for 200 distinct combinations of FVD parameters were rapidly predicted using a trained ANN surrogate model, which maintained high accuracy in predicting the targeted three or four objectives. After prediction, the outcomes were preliminarily evaluated, and candidate solutions underwent crossover and mutation operations. The crossover probability was set to 0.8 and the mutation probability to 0.1. These settings were chosen to balance the convergence rate with the preservation of solution diversity. Over 150 generations, the NSGA-II algorithm executed a total of 30,000 forward evaluations via the ANN surrogate model. This surrogate model-based approach effectively integrates the ANN with the NSGA-II algorithm, yielding significant computational efficiency improvements compared to conventional FE model-based methods, while preserving prediction accuracy.

Figure 18 illustrates the convergence trends of the summed mean normalized responses across generations for both the three-objective and four-objective optimization scenarios. The three-objective optimization focuses on minimizing: (1) pylon top displacement, (2) longitudinal deck displacement, and (3) pylon base shear, while the four-objective optimization introduces an additional goal—minimizing (4) mean bending moment energy. For both strategies, the normalized responses are averaged and aggregated, with rank and diversity assessed at each generation using ranking and crowding distance metrics. Subsequently, crossover and mutation operators are applied to drive the population toward improved Pareto-front solutions. Notably, in both scenarios, the summed mean normalized responses decrease rapidly during the initial stages, followed by a gradual increase before finally stabilizing at a specific value. These trends demonstrate the algorithm's effectiveness in achieving convergence within the design space.

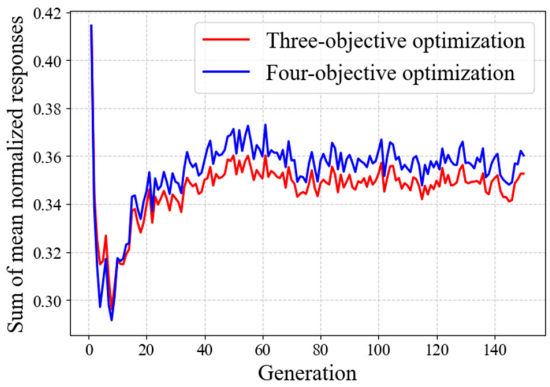


Figure 18. Convergence trends of the sums of mean normalized responses over generations for three-objective and four-objective optimizations.

Specifically, the three-objective optimization process can be visualized within a three-dimensional (3D) response space. Figure 19 demonstrates the evolution of the Pareto front across the 1st, 50th, and 150th generations for the three-objective optimization. Initially, the ANN surrogate model generated a broad 3D Pareto surface from 200 distinct parameter combinations, capturing an extensive design space. As the generation progressed, the Pareto surface gradually converged toward optimized solution sets, achieving convergence by the 150th generation.

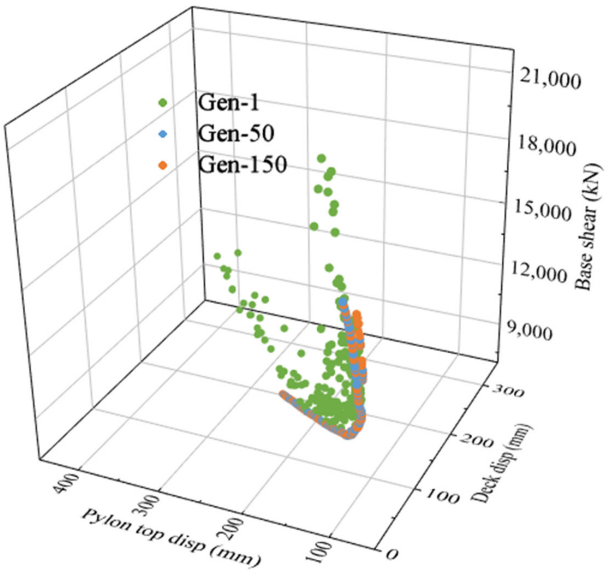


Figure 19. Evolution of Pareto fronts during the 3-objective optimization process.

Within the 3D response space, the Pareto front clearly illustrates the trade-offs among the three objectives and the evolution of responses across successive generations. A strong correlation is observed between pylon top displacement and deck displacement, alongside a clear trade-off between displacement responses and base shear. The optimization process demonstrates rapid convergence within the first 50 generations, after which the solutions become more densely distributed, reflecting a gradual convergence of the Pareto front.

Upon convergence of the Pareto front, the weighted aggregation method was applied to assess and rank the parameter combinations. This approach identified the optimal FVD parameters as K = 928,000 kN/m, C = 3938 kN/(m/s), and α = 0.32. These parameters were subsequently incorporated into the FE model of the case study bridge for nonlinear time-history analyses. The FE simulation yielded a pylon top displacement of 45.2 mm, a deck displacement of 84.8 mm, and a base shear of 11,973.1 kN. Table 10 summarizes the key responses from both the FE simulations and the surrogate model predictions, revealing errors of up to 7.5% for deck displacement, 4.9% for pylon top displacement, and 3.0% for base shear. This indicates that the surrogate model provides predictions closely aligned with the FE simulations, even for FVD parameter combinations unseen in the training dataset.

Table 10. Performance metrics from the FE simulations and the surrogate model.

Performance Metric	ANN Model	FE Model	Error
Deck disp. (mm)	41.8	45.2	7.5%
Pylon top disp. (mm)	80.6	84.8	4.9%
Pylon base shear (kN)	11,611.3	11,973.1	3.0%

Table 11 summarizes the optimized FVD parameters obtained from three optimization strategies: parametric analysis-driven, ANN-based three-objective, and ANN-based four-

objective optimization strategy. For each optimized parameter combination, four seismic responses of the case study bridge were computed via nonlinear time-history analyses. It can be noted that all seismic responses are significantly reduced when the optimized FVD is installed. Among the three optimization strategies, notably improved responses are highlighted in bold, as presented in Table 11.

Table 11. Comparison between three different optimization strategies.

Parameters/Responses	Without FVDs	Parametric Analysis-Driven Optimization	ANN-Based 3-Objective Optimization	ANN-Based 4-Objective Optimization
K (kN/m)	-	1,000,000	928,000	895,000
C (kN·s/m)	-	3000	3938	3947
α	-	0.3	0.32	0.33
Deck disp. (mm)	486.6	54.7	**45.2**	**47.4**
Pylon top disp. (mm)	613.3	92.3	**84.8**	**85.3**
Pylon base shear (kN)	14,600.0	**10,847.8**	11,973.1	**11,884.9**
MBME (kN·m)	121.2	10.1	8.9	**7.7**
Time consuming (min)	-	1500.5	1500.5 + 9.0 + 0.8	1500.5 + 9.0 + 0.8

In the parametric analysis-driven optimization strategy, the pylon base shear is effectively controlled at 10,847.8 kN, the lowest among the three strategies considered. Comparatively, the three-objective optimization strategy achieves a greater reduction in both deck displacement (45.2 mm) and pylon top displacement (84.8 mm), with these values being the smallest among the three strategies. However, this improvement comes with a slight increase in pylon base shear. On the other hand, the four-objective optimization strategy demonstrates a more balanced trade-off across the four responses. While displacement responses exhibit a minor increase (deck displacement: 47.4 mm; pylon top displacement: 85.3 mm), the base shear is notably reduced to 11,884.9 kN compared to the three-objective strategy.

Furthermore, the fourth response (MBME) was analyzed across all three strategies to assess the economic and mechanical rationality of the case study bridge. The smallest MBME value (7.7 kN·m) was achieved in the four-objective strategy, where the MBME was explicitly targeted during the NSGA-II optimization process. Interestingly, the three-objective strategy yielded a relatively low MBME value of 8.9 kN·m, even though it was not directly optimized during the process. This outcome demonstrates the advantage of incorporating the MBME response into the training of the ANN surrogate model, where it served not only as a predicted response but also as a loss penalty with clear physical significance [48]. In comparison, the parametric-analysis-driven strategy produced a higher MBME value of 10.1 kN·m.

Additionally, we compared the computational time required for the three strategies. For consistency, all strategies utilized an identical dataset, with data generation consuming 1500.5 min on a CPU-based computer (Intel i5, 2.90 GHz). Notably, this data generation time can be significantly reduced through parallel computation techniques. The training of the ANN surrogate model required only 9.0 min, while the optimization process itself was completed in approximately 0.8 min for 150 generations. These results demonstrate the efficiency and robustness of the ANN-based multi-objective optimization strategies in both training and optimization phases.

4. Conclusions

This study investigated two methods for optimizing FVD parameters in a case study cable-stayed bridge: a parametric analysis-driven strategy and a surrogate model-based strategy. Key conclusions are:

1. The parametric analysis-driven optimization strategy provides preliminary guidance for selecting optimal FVD parameters. Although this strategy is straightforward and interpretable, it relies heavily on expertise, restricting its ability to explore large design space and its generalization to multi-objective optimization problems.
2. The integration of an ANN surrogate model with the NSGA-II algorithm demonstrated that the ANN-based multi-objective optimization strategy can not only predict multiple seismic responses accurately, but also reduce computational cost during the multi-objective optimization process. This strategy enables efficient exploration of high-dimensional parameter spaces and yields more effective and generalizable solutions.
3. The ANN-based optimization strategy outperformed the parametric analysis-driven strategy by incorporating the MBME loss during surrogate model training. This enhancement improved the fidelity and generalization of the ANN model, demonstrating its potential for addressing high-dimensional, multi-objective optimization challenges.

While this study highlights the feasibility and advantages of the proposed optimization strategies for cable-stayed bridges with FVDs, it is based on several simplifying assumptions. For instance, the structural system is assumed to be linear, excluding considerations of soil-structure interaction and the sag of stay cables. To enhance practical applicability, future research should focus on improving the generalization capabilities of surrogate models. This can be achieved by: (1) expanding training datasets to include additional constraints and diverse parameters, such as varying loading conditions and seismic scenarios; and (2) incorporating nonlinear effects, including soil-structure interaction and cable sagging, to enhance model fidelity in real-world scenarios. These advancements would improve the adaptability of the proposed strategy, enabling it to address more complex and higher-dimensional engineering challenges in engineering practice.

Author Contributions: Q.L.: conceptualization, writing, review and editing, funding acquisition; Z.L.: investigation, software, writing—original draft preparation; J.Z.: investigation, methodology, writing—review and editing; Y.L.: software, methodology; S.Z.: writing—review, and editing, validation, funding acquisition; X.W.: writing—review, and editing, project administration. All authors have read and agreed to the published version of the manuscript.

Funding: This work was supported by the Open Foundation of State Key Laboratory for Strength and Vibration of Mechanical Structure under Grant SV2018-KF-35, the Start-Up Foundation of XUST under Grant 2018YQ2-05, and the Technology Innovation Foundation of CCCC under Grant KCJJ2023-32-07.

Data Availability Statement: Some data or models used during the study are available from the corresponding author by request.

Conflicts of Interest: Shimin Zhu and Xing Wu were employed by CCCC First Highway Consultants Co., Ltd. The remaining authors declare that the research was conducted in the absence of any commercial or financial relationships that could be perceived as a potential conflict of interest.

References

1. Xu, L.; Zhang, H.; Gao, J.; Zhang, C. Longitudinal Seismic Responses of a Cable-Stayed Bridge Based on Shaking Table Tests of a Half-Bridge Scale Model. *Adv. Struct. Eng.* **2019**, *22*, 81–93. [CrossRef]
2. Shen, Y.; Li, Y.; Xu, W.; Li, J. Evaluation of Seismic-Induced Impact Interaction between a Cable-Stayed Bridge and Its Approach Spans Using a Simplified Analysis Model. *J. Earthq. Eng.* **2022**, *26*, 3343–3363. [CrossRef]
3. Xie, W.; Sun, L. Transverse Seismic Response and Failure Mode of Towers of a Cable-Stayed Bridge Full-Model: Tests and Simulations. *Eng. Fail. Anal.* **2021**, *122*, 105224. [CrossRef]
4. Zhu, J.; Zhang, W.; Zheng, K.F.; Li, H.G. Seismic Design of a Long-Span Cable-Stayed Bridge with Fluid Viscous Dampers. *Pract. Period. Struct. Des. Constr.* **2016**, *21*, 04015006. [CrossRef]
5. Ali, H.M.; Abdel-Ghaffar, A.M. Seismic Energy Dissipation for Cable-stayed Bridges Using Passive Devices. *Earthq. Eng. Struct. Dyn.* **1994**, *23*, 877–893. [CrossRef]

6. Guo, W.; Zeng, C.; Xie, X.; Bu, D. Pseudodynamic Hybrid Simulation of High-Speed Railway Bridge-Track System with Rotational Friction Damper. *Int. J. Struct. Stab. Dyn.* **2020**, *20*, 2040014. [CrossRef]
7. Leblouba, M. Selection of Seismic Isolation System Parameters for the Near-Optimal Design of Structures. *Sci. Rep.* **2022**, *12*, 14734. [CrossRef]
8. De Domenico, D.; Ricciardi, G.; Takewaki, I. Design Strategies of Viscous Dampers for Seismic Protection of Building Structures: A Review. *Soil Dyn. Earthq. Eng.* **2019**, *118*, 144–165. [CrossRef]
9. Soneji, B.B.; Jangid, R.S. Passive Hybrid Systems for Earthquake Protection of Cable-Stayed Bridge. *Eng. Struct.* **2007**, *29*, 57–70. [CrossRef]
10. Calvi, G.M.; Sullivan, T.J.; Villani, A. Conceptual Seismic Design of Cable-Stayed Bridges. *J. Earthq. Eng.* **2010**, *14*, 1139–1171. [CrossRef]
11. Camara, A.; Astiz, M.A. Analysis and Control of Cable-Stayed Bridges Subject to Seismic Action. *Struct. Eng. Int.* **2014**, *24*, 27–36. [CrossRef]
12. Martínez-Rodrigo, M.D.; Filiatrault, A. A Case Study on the Application of Passive Control and Seismic Isolation Techniques to Cable-Stayed Bridges: A Comparative Investigation through Non-Linear Dynamic Analyses. *Eng. Struct.* **2015**, *99*, 232–252. [CrossRef]
13. Ruangrassamee, A.; Kawashima, K. Seismic Response Control of a Cable-Stayed Bridge by Variable Dampers. *J. Earthq. Eng.* **2006**, *10*, 153–165. [CrossRef]
14. Vader, T.S.; McDaniel, C.C. Influence of Dampers on Seismic Response of Cable-Supported Bridge Towers. *J. Bridge Eng.* **2007**, *12*, 373–379. [CrossRef]
15. Zhang, X.-J.; Zhao, C.-Y.; Guo, J. Investigation of Seismic Performance of Super Long-Span Cable-Stayed Bridges. *Earthq. Struct.* **2018**, *14*, 493–503.
16. Chang, C.-M.; Loh, C.-H. Seismic Response Control of Cable-Stayed Bridge Using Different Control Strategies. *J. Earthq. Eng.* **2006**, *10*, 481–508. [CrossRef]
17. Ali, H.E.M.; Abdel-Ghaffar, A.M. Seismic Passive Control of Cable-Stayed Bridges. *Shock. Vib.* **1995**, *2*, 259–272. [CrossRef]
18. Zoccolini, L.; Bruschi, E.; Pettorruso, C.; Rossi, D.; Quaglini, V. Fluid Viscous Dampers for Seismic Protection of Bridges: A State of the Art. *Procedia Struct. Integr.* **2024**, *62*, 669–676. [CrossRef]
19. He, X.; Yang, Y.; Xiao, X.; Deng, Y. Research on Fluid Viscous Damper Parameters of Cable-Stayed Bridge in Northwest China. *Shock. Vib.* **2017**, *2017*, 4532325. [CrossRef]
20. Feng, D.; Wang, J. Seismic Control of a Self-Anchored Suspension Bridge Using Fluid Viscous Dampers. *Int. J. Struct. Stab. Dyn.* **2021**, *21*, 2150025. [CrossRef]
21. Wu, C.; He, X.; He, L.; Zhao, X.; Wang, Y.; Li, C.; Yang, Y.; Zhang, X. Improving Cable-Stayed Bridge Longitudinal Aseismic Capability via Fluid Viscous Damper Parametric Optimization and Experimental Investigation. *Structures* **2023**, *57*, 105199. [CrossRef]
22. Wen, J.; Han, Q.; Xie, Y.; Du, X.; Zhang, J. Performance-Based Seismic Design and Optimization of Damper Devices for Cable-Stayed Bridge. *Eng. Struct.* **2021**, *237*, 112043. [CrossRef]
23. Xu, L.; Bi, K.; Gao, J.-F.; Xu, Y.; Zhang, C. Analysis on Parameter Optimization of Dampers of Long-Span Double-Tower Cable-Stayed Bridges. *Struct. Infrastruct. Eng.* **2020**, *16*, 1286–1301. [CrossRef]
24. Liu, Q.; Geng, J.; Wang, Y.; Ge, Y.; Bao, Q. Multi-Parameter Damper Optimization of Cable-Stayed Bridge Considering Energy Dissipation. *J. Phys. Conf. Ser.* **2023**, *2541*, 012002. [CrossRef]
25. Chen, X.; Spencer, B.F.; Li, J.; Guan, Z.; Pang, Y. Optimization of Distribution Patterns of Link Beams in a Double-column Tall Pier Bent Subjected to Earthquake Excitations. *Earthq. Eng. Struct. Dyn.* **2023**, *52*, 641–659. [CrossRef]
26. Baei, M.; Terzic, V. Optimal Design of Dampers in Seismic Applications Utilizing the MOPSO Algorithm. *Front. Built Environ.* **2022**, *8*, 1040129. [CrossRef]
27. Sun, C.; Wang, K.; Liu, Q.; Wang, P.; Pan, F. Machine-Learning-Based Comprehensive Properties Prediction and Mixture Design Optimization of Ultra-High-Performance Concrete. *Sustainability* **2023**, *15*, 15338. [CrossRef]
28. Guo, W.; He, Y.; Zhu, Y.; Hu, Y. Performance Parameter Design of Seismic Isolation Bearings for High-Speed Railway Simply-Supported Bridges Using Neural Network. *Soil Dyn. Earthq. Eng.* **2024**, *179*, 108535. [CrossRef]
29. Fang, C.; Ping, Y.; Gao, Y.; Zheng, Y.; Chen, Y. Machine Learning-Aided Multi-Objective Optimization of Structures with Hybrid Braces—Framework and Case Study. *Eng. Struct.* **2022**, *269*, 114808. [CrossRef]
30. Jiang, M.; Rui, X.; Yang, F.; Zhu, W.; Zhang, Y. Multi-Objective Optimization Design for a Magnetorheological Damper. *J. Intell. Mater. Syst. Struct.* **2022**, *33*, 33–45. [CrossRef]
31. Yang, G.; Zhang, T.; Mao, J.; Tian, L.; Du, Y. A NSGA-II-Based Approach for Optimizing Structural Component Pre-Reinforcement to Enhance Cable-Stayed Bridge Resilience. *Adv. Struct. Eng.* **2024**, *28*, 1075–1092. [CrossRef]
32. Tian, Z.; Zhang, Z.; Ning, C.; Peng, T.; Guo, Y.; Cao, Z. Multi-Objective Optimization of Cable Force of Arch Bridge Constructed by Cable-Stayed Cantilever Cast-in-Situ Method Based on Improved NSGA-II. *Structures* **2024**, *59*, 105782. [CrossRef]

33. Almutairi, A.; Lu, J.; Wang, N.; Elgamal, A. *Analysis of Multi-Span Bridges Using OpenSees*; National Academies: Washington, DC, USA, 2016.
34. Rastgoo Moghadam, S.; Konstantinidis, D. Experimental and Analytical Studies on the Horizontal Behavior of Elastomeric Bearings under Support Rotation. *J. Struct. Eng.* **2021**, *147*, 04021024. [CrossRef]
35. Kalfas, K.N.; Ghorbani Amirabad, N.; Forcellini, D. The Role of Shear Modulus on the Mechanical Behavior of Elastomeric Bearings When Subjected to Combined Axial and Shear Loads. *Eng. Struct.* **2021**, *248*, 113248. [CrossRef]
36. Joyner, M.D.; Gardner, C.; Puentes, B.; Sasani, M. Resilience-Based Seismic Design of Buildings through Multiobjective Optimization. *Eng. Struct.* **2021**, *246*, 113024. [CrossRef]
37. Deutsch, J.L.; Deutsch, C.V. Latin Hypercube Sampling with Multidimensional Uniformity. *J. Stat. Plan. Inference* **2012**, *142*, 763–772. [CrossRef]
38. Akiba, T.; Sano, S.; Yanase, T.; Ohta, T.; Koyama, M. Optuna: A Next-Generation Hyperparameter Optimization Framework 2019. In Proceedings of the 25th ACM SIGKDD International Conference, Anchorage, AK, USA, 4–8 August 2019.
39. Verma, S.; Pant, M.; Snasel, V. A Comprehensive Review on NSGA-II for Multi-Objective Combinatorial Optimization Problems. *IEEE Access* **2021**, *9*, 57757–57791. [CrossRef]
40. Jia, H.; Liu, Z.; Xu, L.; Bai, H.; Bi, K.; Zhang, C.; Zheng, S. Dynamic Response Analyses of Long-Span Cable-Stayed Bridges Subjected to Pulse-Type Ground Motions. *Soil Dyn. Earthq. Eng.* **2023**, *164*, 107591. [CrossRef]
41. *JTG D20—2017*; Specifications for Seismic Design of Highway Bridges. Standards Press of China: Bejing, China, 2020.
42. Kamrava, A. Comparing Results of MATLAB and Seismosignal in Plotting Earthquake Graphs. *Curr. World Environ.* **2015**, *10*, 11–14. [CrossRef]
43. Ras, A.; Boumechra, N. Seismic Energy Dissipation Study of Linear Fluid Viscous Dampers in Steel Structure Design. *Alex. Eng. J.* **2016**, *55*, 2821–2832. [CrossRef]
44. Liu, Q.; Zhu, S.; Yu, W.; Wu, X.; Song, F.; Ren, X. Ground Motion Frequency Insensitivity of Bearing-Supported Pedestrian Bridge with Viscous Dampers. *KSCE J. Civ. Eng.* **2021**, *25*, 2662–2673. [CrossRef]
45. Panda, S.K.; Jana, P.K. Efficient Task Scheduling Algorithms for Heterogeneous Multi-Cloud Environment. *J. Supercomput.* **2015**, *71*, 1505–1533. [CrossRef]
46. Marler, R.T.; Arora, J.S. The Weighted Sum Method for Multi-Objective Optimization: New Insights. *Struct. Multidisc. Optim.* **2010**, *41*, 853–862. [CrossRef]
47. Yu, C.; Xiang, H.; Li, Y.; Pan, M. Optimization of Longitudinal Viscous Dampers for a Freight Railway Cable-Stayed Bridge under Braking Forces. *Smart Struct. Syst.* **2018**, *21*, 669–675.
48. Ozdagli, A.; Volgyesi, P.; Koutsoukos, X. Surrogate Modeling Using Physics-Guided Learning. In Proceedings of the Cyber-Physical Systems and Internet of Things Week 2023, San Antonio, TX, USA, 9 May 2023; ACM: New York, NY, USA, 2023; pp. 130–135.

Disclaimer/Publisher's Note: The statements, opinions and data contained in all publications are solely those of the individual author(s) and contributor(s) and not of MDPI and/or the editor(s). MDPI and/or the editor(s) disclaim responsibility for any injury to people or property resulting from any ideas, methods, instructions or products referred to in the content.